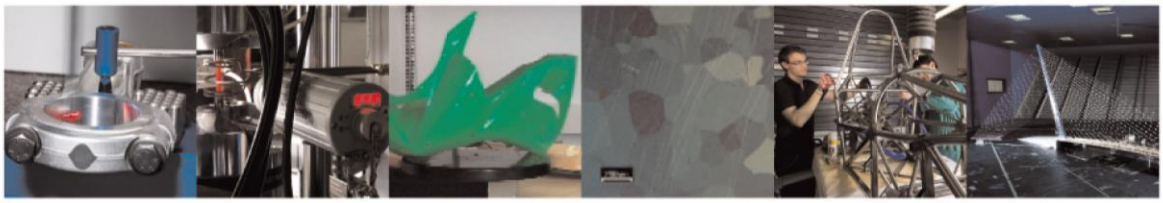

In situ monitoring of selective laser melting of zinc powder via infrared imaging of the process plume

Grasso, M.; Demir, A. G.; Previtali, B.; Colosimo, B. M.

This is a post-peer-review, pre-copyedit version of an article published in ROBOTICS AND COMPUTER-INTEGRATED MANUFACTURING. The final authenticated version is available online at: http://dx.doi.org/10.1016/j.rcim.2017.07.001

DIPARTIMENTO DI MECCANICA ■ POLITECNICO DI MILANO
via G. La Masa, 1 ■ 20156 Milano ■ EMAIL (PEC): pecmecc@cert.polimi.it
http://www.mecc.polimi.it
Rev. 0

In situ Monitoring of Selective Laser Melting of Zinc Powder via Infrared Imaging of the Process Plume

M. Grasso[1], A. G. Demir, B. Previtali, B. M. Colosimo

Dipartimento di Meccanica, Politecnico di Milano

Via La Masa 1, 20156 Milan (Italy)

marcoluigi.grasso@polimi.it; aligokhan.demir@polimi.it; barbara.previtali@polimi.it;

biancamaria.colosimo@polimi.it

Abstract. *Despite continuous technological improvements in metal additive manufacturing (AM) systems, process stability is still affected by several possible sources of defects especially in the presence of challenging materials. Thus, both the research community and the major AM system developers have focused an increasing attention on in situ sensing and monitoring tools in the last years. However, there is still a lack of statistical methods to automatically detect the onset of a defect and signal an alarm during the part's layer-wise production. This study contributes to this framework with two levels of novelty. First, it presents an in situ monitoring method that integrates the acquisition of infrared images with a data mining approach for feature extraction and a statistical process monitoring technique to design a data-driven and automated alarm rule. Second, the method is monitors powder bed fusion processes for difficult-to-process materials like zinc and its alloys, which impose several challenges to the process stability and quality because of their low melting and boiling points. To this aim, the proposed approach analyzes the byproducts generated by the interaction between the energy source and the material. In particular, it detects unstable behaviors by analyzing the salient properties of the process plume to detect unstable melting conditions. This case study entails an SLM process on zinc powder, where different sets of process parameters were tested leading either to in-control or out-of-control quality conditions. A comparison analysis highlights the effectiveness of plume-based stability monitoring.*

Keywords: metal additive manufacturing; selective laser melting; in situ monitoring; infrared imaging; zinc; process plume.

1 Introduction

Selective laser melting (SLM) is an additive manufacturing (AM) process to produce metal parts via powder bed fusion. This kind of process provides great flexibility for the production of highly customized items, lightweight structures, innovative shapes, parts with complicated internal channels, etc. [1 – 9]. A laser is used to locally melt a thin layer of metal powder (e.g.,

[1] Corresponding author

about $40 - 50\ \mu m$) deposited on a flat substrate along a predefined scanning path. Once the SLM process of a full slice has been realized, the substrate is lowered, and a new layer of powder is deposited, and the next slice is scanned. For an overview of the process and the related technology, the interested reader may refer to the literature [1]. The accuracy of the produced parts—together with their mechanical and physical properties—make this kind of process suitable for the production of functional parts in several sectors (healthcare, aerospace, automotive, tooling and molding, etc.) [1 - 4]. In addition, the possibility of producing structures and free-form shapes that are difficult or even impossible to produce with other existing technologies makes SLM systems industrially attractive for a wide range of innovative applications.

However, different quality-related issues still affect the capability, stability and repeatability of the process. Local defects may occur during the layer-wise production of the part: the root causes may include improper process parameters, insufficient supports, a non-homogeneous powder deposition, improper heat exchanges, material contaminations, etc. [10 - 15]. A rapidly increasing literature in this framework has been devoted to the development of in-process monitoring tools [10 - 15]. These methods involve *indirect* measurements based on in situ sensors of quantities related to the final part quality rather than relying on direct (post-process) quality inspections. Indeed, the fast recognition of an out-of-control state is important to abort the SLM process as soon as possible saving time and preventing waste of expensive material. It is also important to implement novel feedback control strategies to mitigate the propagation of defects and, when possible, to recover from the unstable condition in a first-time-right oriented framework.

With few exceptions, in situ SLM monitoring methods proposed in the literature can be divided into two groups: (i) co-axial monitoring of the melt pool via in situ sensors by exploiting the optical path of the laser [16 - 28] and (ii) off-axial monitoring devoted to other categories of signatures measured by sensors placed outside the laser optical path [29 - 43]. The melt pool properties (i.e., size, shape and temperature profile) are important proxies of the SLM process quality and stability. They have attracted a wide range of research interest in recent years within the metal AM community. However, off-axis sensors offer additional information including the

geometry and temperature profile over the entire track, the amount of ejected material and side-products, the powder bed homogeneity, the geometry and topography of the scanned slice, etc.

Most studies have focused on in situ sensing and data acquisition solutions, but there is still a lack of monitoring methods to automatically detect the onset of the defect and to signal an alarm during the layer-wise production of the part [12]. The first contribution of this study is an automated and data-driven tool to detect process instabilities, which inherits the signal-based process monitoring perspective adopted in the industrial statistics framework [44] and extends it to AM applications. The proposed method is based on the continuous acquisition of infrared (IR) images via an off-axis mounted thermal camera. The method integrates a data mining approach for image segmentation and extraction of relevant information within the regions of interest with a statistical process monitoring technique that allows the design of a data-driven and automated alarm rule. This approach is used for defect detection in the presence of thermally sensitive materials that produce larger amounts of metallic vapor and byproducts than other materials with a possible detrimental effect on the SLM process stability.

Zinc and its alloys belong to this category: They constitute a new family of biodegradable alloys for biomedical devices whose use in AM applications has been gaining an increasing interest [45]. However, due to their low melting and boiling points, the SLM of zinc powder produces large quantities of plume, which differs from the surrounding atmosphere in terms of chemical composition, temperature and pressure. In fact, during the SLM process, partial material vaporization may occur: King *et al*. [46] reported the formation of plasma due to the ionization of the metallic vapor and the surrounding gas. Further vapor formation and heating of the surrounding gas forms the process plume. The plume can induce changes in the optical properties of the beam path, which may alter the beam profile and energy density on the material's surface [47]. Moreover, heat accumulations and thermal drifts during the process can change the plume quantity and form. This yields detrimental effects on the process stability that may lead to poor part quality—especially regarding the internal and sub-surface porosity [48].

Many groups have investigated the plume properties in laser welding [49 - 52] and metal AM [53 - 54], but, to the best of our knowledge, such an information has never been used for

monitoring purposes in SLM. On the contrary, this study is the first attempt to develop an in situ monitoring methodology that relies on the analysis of the process plume properties as proxies of the SLM process stability to detect unstable melting conditions since their early stage. Thermal images are segmented to extract the region of interest (ROI) that includes the plume emission. Then, a multivariate control-charting scheme is proposed to monitor the selected ROI statistical descriptors (i.e., the area and the mean intensity) to rapidly detect departures from a stable pattern in terms of plume emissions.

We compare different segmentation algorithms and propose an automated rule to isolate the ROI from the rest of the image. A case study is presented that consists of an SLM process on zinc powder where both stable and unstable melting conditions were observed. The results show that the plume descriptors can determine the stability of the process and anticipate the departure from in-control (stable) behaviors. The proposed method is compared against benchmark competitors to highlight the benefits and resulting performance.

Section 2 presents the experimental setup adopted during the SLM of zinc powder in the presence of both stable and unstable melting conditions; Section 3 describes the image pre-processing and process monitoring steps of the proposed approach; Section 4 presents a discussion of the results; and Section 5 concludes the paper.

2 Experimental setup

Zinc and its alloys are the newest family of materials in biodegradable metals. Biodegradability refers to the dissolution of the medical device inside the human body once it fulfills its duty [55]. This property is especially appealing in cardiovascular stents. The recently developed attention on zinc is due to a biodegradation rate that is slower than Mg- and Fe-based alloys [45]. The use of zinc in additive manufacturing processes has not received much attention so far due to the restricted applications of the pure metal and its alloys. Moreover, pure zinc is highly problematic within the SLM process because of its very low melting ($T_m = 693\ K$) and vaporization ($T_v = 1180\ K$) points [48]. These characteristics render the processability of zinc and its alloys particularly difficult due to the excessive vapor and plume generation. The process

can be stabilized provided adequate solutions to eliminate the particle accumulation in the processing chamber. Within stable operating conditions, pure zinc shows a peculiar type of defect consisting of partial disintegration at high energy density levels. The defect does not manifest immediately, but occurs after a certain number of layers have been deposited with consecutive heat accumulation. As a result, a material burst is observed during the melting of a layer, and it yielded a disintegration of the previously built layers [56]. Such a defect can be avoided by an adequate choice of processing parameters. However, heat accumulation depends on the form and the size of the scanned geometry and prevents excessive accumulation within the entire build; this is a difficult task in practice. In particular, thinner sections are known to be more prone to such phenomenon. Therefore, it is important to control the process evolution via process monitoring tools to quickly detect unstable behaviors.

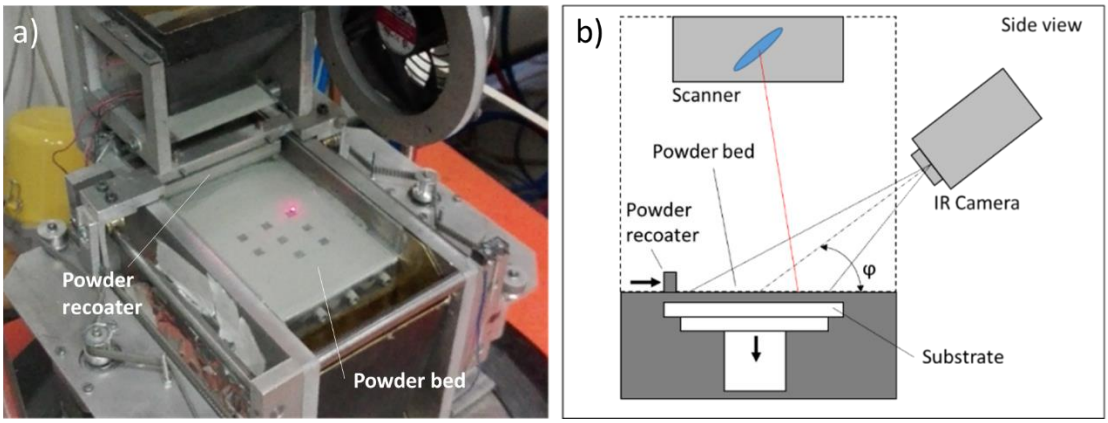

Fig. 1 – a) A view of the building chamber of the SLM system prototype used for the experimental activity; b) side view of the IR camera setup.

In our case study, we used a prototype SLM system named the Powderful (Fig. 1, left panel). The system is composed of a multimode fiber laser source with 1 kW maximum power (IPG Photonics YLR-1000, Cambridge, MA, USA) coupled to a scanner (El.En. Scan Fiber, Florence, Italy). The scan path trajectory was designed with the LogoTag software (Taglio, Piobesi D'alba, Italy). Cubic specimens of size $5 \times 5 \times 5\ mm$ were realized with different sets of process parameters. In particular, the laser power (P), the scan speed (v) and the hatch distance between the consecutive scan lines (h) were modified. A fixed scan direction was applied at each layer

corresponding to a pathway from left to right within the field of view of the thermal camera. The parameter sets (see Table 1) have been divided into three categories, hereafter named Scenario 1, 2 and 3 depending on the observed quality of the final parts. In Scenario 1, three sets of parameters were tested, and all of them yielded a stable process with in-control quality properties of the final parts. Scenario 2 and 3 are unstable process conditions that yielded part disintegration after a certain amount of layers. In these conditions, specimens could be built to around 3 mm height after which the previously built layers collapsed with a burst of material from the surface.

Table 1 – SLM process parameters used different scenarios.

Fixed parameters		**Values**			
Focal position, Δz (mm)		0			
Layer thickness, t (μm)		50			
Scenario-dependent parameters		Laser power, P (W)	Scan speed, v (mm/s)	Hatch distance, h (μm)	Apparent density, ρ_a (%)
Scenario 1	Set 1	110	475	160	96.2±1.2
	Set 2	195	679	160	98.4±1.3
	Set 3	195	475	160	98.7±0.4
Scenario 2		195	475	78	n/a
Scenario 3		195	270	160	n/a

The specimens are shown in Fig. 2. Fig. 3 presents a representative cross-section image of the samples obtained in Scenario 1. The specimens are characterized by a small fraction in porosity dispersed around the area. The apparent density was measured over optical microscopy images. The density values ranged between 96.2% and 98.7% under in-control scenarios; density could not be measured for out-of-control scenarios. Scenario 1 is used in the next section to illustrate the different steps of the proposed approach and as a reference for a comparison analysis against benchmark methods. Scenario 2 and 3 are used in Section 4 to discuss the performances of our proposed approach in the presence of out-of-control quality conditions.

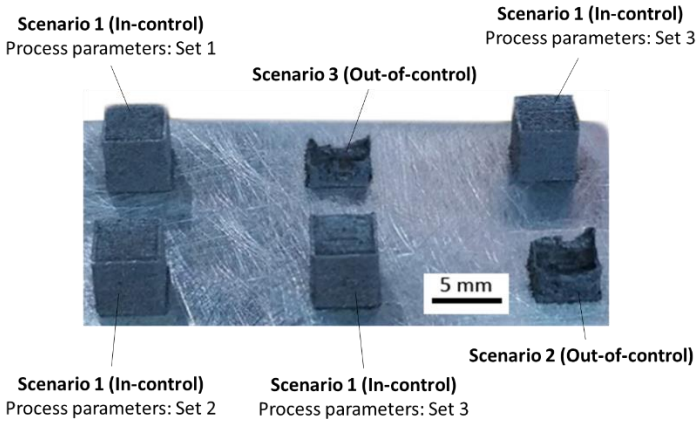

Fig. 2 – Specimens produced under in-control (Scenario 1) and out-of-control (Scenario 2 and 3) SLM process conditions.

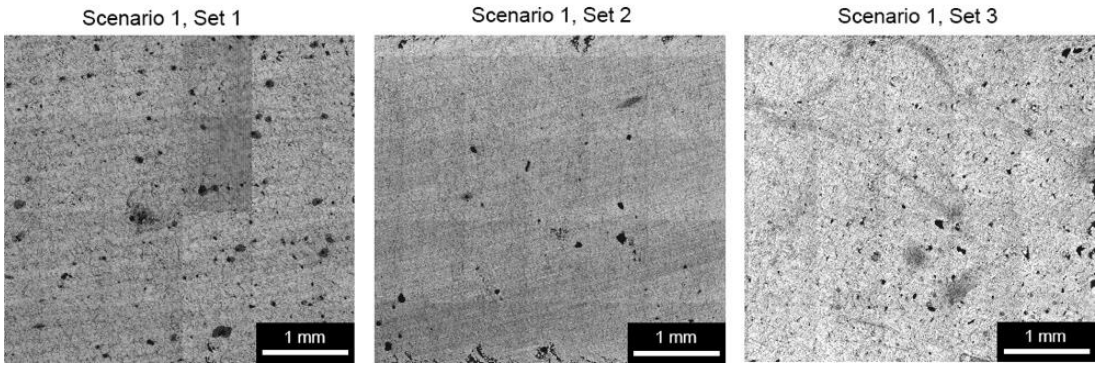

Fig. 3 – Cross section images of the samples obtained with in control processing conditions (Scenario 1).

Infrared images were acquired via a FLIR SC3000 with a spectral range of 8 – 9 μm placed at about $\varphi = 30°$ above the powder bed with a sampling frequency $f_s = 50Hz$, a spatial resolution of 320×240 pixels, and an approximated temperature range of 100 – 500 °C (Fig. 1, right panel). The sampling frequency was chosen as a compromise between the capability of properly characterizing the shape/size evolution of the ROI during the scanning of each slice, the spatial resolution of the ROI representation and analysis, and the computational cost needed for image processing and in-process monitoring. The emissivity of the monitored object needs to be known to achieve absolute temperature measurements via IR imaging. However, this coefficient is typically difficult to determine due to the physical transformations that the material undergoes during the SLM process, i.e., from powder to molten form and then from molten to solid form

[10 – 11]. Thus, a rough calibration was applied considering only the emissivity of the material in its solid state. This allowed us to represent the pattern of the temperature intensity map within each frame for spatial and temporal temperature variation analysis rather than acquiring point-wise temperature measurements. The thermal images were then normalized into a gray scale pixel intensity map ranging from 0 (black - cold) to 1 (white - hot) for image segmentation purposes.

In each scenario, the dataset consists of IR image streams acquired during the SLM of 14 non-consecutive layers. The first four monitored layers are spaced two layers apart, and they belong to the bottom of the cubic specimens (in the height range 0.2 – 0.5 mm from the substrate along the build direction). They were used as a training phase for our proposed approach under the assumption that unstable melting produces a departure from in-control conditions that grow over time layer to layer. Generally speaking, the choice of the number of layers to be used as a training phase should result from a compromise between the reactivity of the monitoring tool and the need to collect a sufficient amount of data to reliably start monitoring the process.

The next ten monitored layers are spaced five layers apart 0.5 – 3 mm from the substrate. The collapse of cubes in Scenario 2 and 3 became evident in the last layers especially in Scenario 3 where the plume emissions considerably increased eventually leading to a disintegration of previously melted layers that generated a visible material ejection accompanied by an increase in the plume quantity (see Section 4). However, the aim of the proposed methodology anticipates detection of process instability by signaling an out-of-control condition since its onset stage. The process was intentionally continued to observe the unstable growth over time. This was aborted only after partial disintegration. In contrast, Scenario 1 had no process interruption, and all parts were produced.

3 Image segmentation and process monitoring

The IR image stream acquired during the SLM process can be represented as a 3-dimensional array, $\boldsymbol{\mathcal{U}} \in \mathbb{R}^{J \times M \times N}$, where J is the total number of acquired frames, and $M \times N$ is the size of each frame in pixels. The 3-dimensional array $\boldsymbol{\mathcal{U}}$ is such that $\boldsymbol{\mathcal{U}} = \{\boldsymbol{U}_1, \boldsymbol{U}_2, \dots, \boldsymbol{U}_J\}$ where $\boldsymbol{U}_j \in \mathbb{R}^{M \times N}$ is the j^{th} frame of size $M \times N$, and $j = 1, \dots, J$.

The overall array can be divided into a training set, $\boldsymbol{\mathcal{U}}_I = \{\boldsymbol{U}_1, \boldsymbol{U}_2, \dots, \boldsymbol{U}_K\}$, and a monitoring set, $\boldsymbol{\mathcal{U}}_{II} = \{\boldsymbol{U}_{K+1}, \boldsymbol{U}_{K+2}, \dots, \boldsymbol{U}_J\}$. The training set includes the frames acquired in a small number of initial layers whereas the monitoring set includes all the remaining frames. Each frame, $\boldsymbol{U}_j$, represents an IR image characterized by a dark (cold) background and multiple hot foreground regions either corresponding to the plume, the laser heated zone (LHZ), or the spatters. The LHZ is the light-emitting region of the slice whose temperature is affected by the transition of the laser spot along its predefined scanning path, whereas the plume originates from that zone and extends above the slice. In this study, the process monitoring approach is focused on the plume. Thus, the spatters are filtered out and are not included into the design of the monitoring scheme. Generally speaking, the region of interest (ROI) consists of the union of the plume and the LHZ because these two regions are partially overlapped in most frames (further details about the aspect of the ROI are provided below). Although the spatters could be, in principle, potential sources of information, their analysis would require considerably higher sampling frequencies to follow their motion and properly describe their generation mechanism. A comparison with methods that include the spatters among the monitored features is discussed in Section 4. Future research will consider the spatters as additional information sources via different in situ sensing setups (a first study on this topic can be found in [57]).

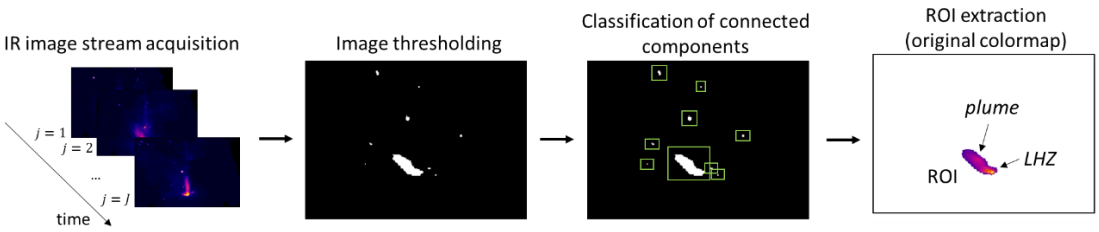

Fig. 4 – Image processing steps for ROI extraction

Fig. 4 shows the sequence of operations to segment the images and extract the ROI. The two major steps involve image thresholding and the classification of the connected components[2].

[2] A connected component is a set of connected pixels that constitute the ROI or other foreground objects (i.e., the spatters).

These are discussed in sub-section 3.1. The computation of ROI statistical descriptors and the design of the process-monitoring tools are discussed in sub-sections 3.2.

3.1 Image thresholding and ROI classification

Image thresholding is necessary to separate the foreground components (i.e., ROIs and spatters) from the background as a preliminary step for subsequent classification and statistical descriptor computation. In [58], thresholding methods are divided into the following categories: histogram-based, clustering-based, entropy-based, attribute-based, spatial and local approaches. A comparison of most of them in different benchmark applications was discussed in [58 - 59] where the authors pointed out that the choice of the most suitable technique is problem-dependent because the achieved performances depend on the nature and properties of the target image.

As far as bi-level thresholding is concerned (as in the present study), the most commonly used approach consists of converting the color image to grayscale and then applying gray level thresholding techniques [60]. Although an exhaustive comparison of the large number of existing methods goes beyond the scope of this study, the most popular approaches available in commercial image processing toolboxes were considered. These include: (1) the IsoData algorithm [61], which is the default choice in the open-source ImageJ software, (2) the Otsu's method [62], which is the default choice in the Matlab Image Processing Toolbox, (3) the Li's minimum cross entropy method [63], (4) the Huang's fuzzy thresholding method [64], and (5) the k-means clustering-based thresholding [65]. All of these methods aim to find an optimal threshold value depending on the specific target function. An example of thresholding results for one IR image of our dataset is shown in Fig. 5, where the left-oriented plume emission is clearly visible. The optimal threshold value is denoted by T. All compared methods provide similar results in this case.

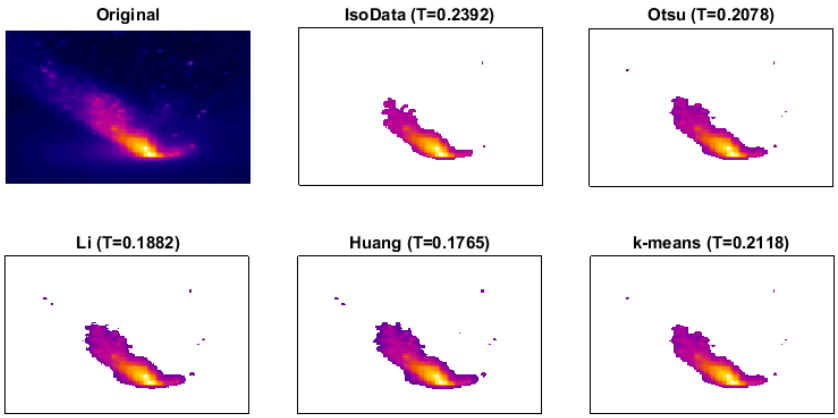

Fig. 5 – Top-left panel: Example of IR image where the plume is evident; Other panels: segmentation results based on IsoData, Otsu's, Li's, Huang's and k-means methods

A larger difference among the competing methods was observed in the presence of frames where the plume was small or even absent as in Fig. 6. As an example, the original image in Fig. 6 top-left panel exhibits a LHZ and eight big spatters. The Otsu's, Li's and k-means methods provided the best results in this case where both the LHZ and the spatters were clearly extracted from the background. Avoiding improper segmentations like the ones provided by IsoData and Huang's methods is important to prevent false alarms caused by image processing errors during in situ monitoring.

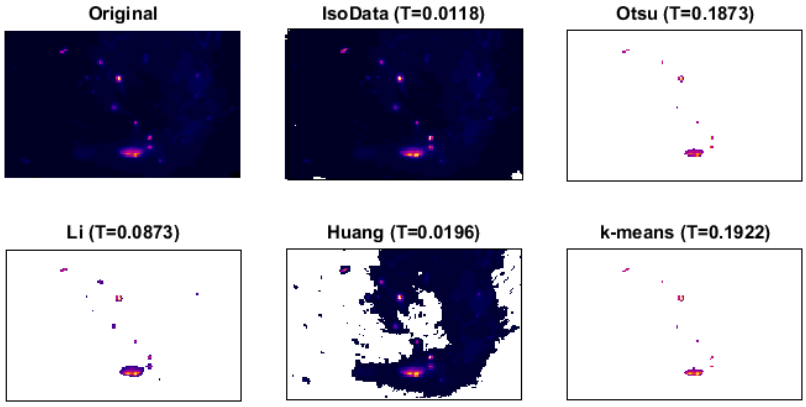

Fig. 6 – Top-left panel: Example of IR image where only the LHZ and the spatters are evident; Other panels: Segmentation results based on IsoData, Otsu's, Li's, Huang's, and k-means methods.

The Otsu's method and the k-means clustering implement different optimization strategies but they share the same criterion [66], and this explains why they yield similar results. However, the Otsu's method avoids the risk of convergence to local minima depending on cluster initialization. In this study, we applied Otsu's method, which yielded very good results for all acquired video frames.

The step after image segmentation consists of identifying the ROI by separating it from the spatters. In the laser welding literature, some authors [49 - 51] applied a classification simply based on the area of the connected components. The components with smaller area than a given threshold were classified as spatters and filtered out. However, no automated method for the choice of this threshold, hereafter denoted by S, was proposed in the literature. In this study, we propose a data-driven rule to estimate S, which relies on the following two considerations. First, the smaller is the value of S, and a larger number of connected components are classified as an ROI in one single frame. Hence, there is a higher probability of a misclassification. On the other hand, larger values of S result in a larger number of frames where no connected component is classified as a ROI due to filtering out both the spatters and the ROI. Let $P_1(S)$ be the percentage of frames belonging to the training set where more than one connected component has been classified as ROI. Let $P_2(S)$ be the percentage of frames belonging to the training set where no connected component has been classified as an ROI. $P_1(S)$ is a monotone decreasing function of S whereas $P_2(S)$ is a monotone increasing function of S. Thus, the best compromise between the two percentages corresponds to the intersection of the two curves. The corresponding value of the threshold is the one we suggest for the ROI extraction in every monitored frame.

Fig. 7 shows the $P_1(S)$ and $P_2(S)$ functions computed in the range $S \in [10 - 100]$ for the monitored layers belonging to the training phase of Scenario 1. In this case, the optimal choice is $S = 64$ pixels. When more than one connected component is classified as an ROI in one single frame, then the ROI is defined as the union of all of them. This is also done to cope with the possible occurrence of bi-modal ROIs, i.e., ROIs divided into two distinct regions of the IR image. Bi-modal ROIs were observed in some cases where the plume was separated from the LHZ.

The choice of S is completely data-driven, and hence the estimation of S is part of the calibration procedure that is carried out during the training phase of the monitoring algorithm.

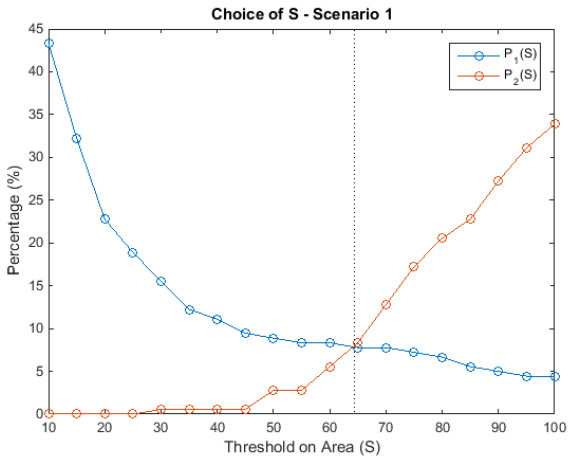

Fig. 7 – $P_1(S)$ and $P_2(S)$ curves in Scenario 1. The vertical dotted line corresponds to the best compromise choice of S according to the proposed approach.

3.2 Statistical descriptors estimation and control chart design

After the image segmentation and ROI classification steps, suitable statistical descriptors can be computed to determine the stability over time of the plume emissions. Despite a lack of studies in the SLM literature about plume descriptors, literature on laser welding or direct energy deposition provides some results that can be extended to SLM processes. In particular, a few previous studies [49 - 51] have shown that the descriptor of main interest to be related to the process stability is the size of the plume (either expressed in terms of its area or its height, which are two strongly correlated quantities). Indeed, a large plume can deflect and absorb the laser beam energy, which changes the beam geometry and energy density reaching the material surface. However, in the case of temperature sensitive materials such as zinc the size of the plume is also expected to be a proxy for the heat accumulation. Moreover, zinc is highly prone to vaporization under laser irradiance as demonstrated in laser welding operations [67].

The peculiar process instability during the SLM of zinc is related to a partial disintegration phenomenon that can be linked to bubble formation and pressure increase around the process zone [68]. Thus, the plume size can be used as a direct indicator to signal the onset of this phenomenon.

In this study, the area of the j-th ROI, A_j, can be approximated by the number of pixels, n_j, included into the ROI, $A_j = n_j$, $j = 1,2, \ldots$. The temperature of the ROI is one additional descriptor of interest. In the absence of ionization, the increased temperature can be linked to the increased amount of material vaporization and heating of the surrounding gas. Despite being strictly related to the energy input to the material, the plume size and its temperature do not necessarily provide the same type of information. Apart from the energy input, the plume size can be affected by pressure field variations, and the gas flow and the scan direction [69 - 70]. On the other hand, the average temperature also depends on the plume composition and the possible occurrence of ionization. Hence, in some cases, different plume temperatures can be achieved with a similar plume size. Thus, a second descriptor is proposed, which consists of the average intensity of all the pixels belonging to the ROI, $\overline{I_j} = \sum_{i \in ROI_j} \frac{I_i}{n_j}$, $j = 1,2, \ldots$. As an example, the bivariate scatterplot of the two descriptors, A_j and $\overline{I_j}$, computed during both the training phase and the monitoring phase of Scenario 1 are shown in Fig. 8.

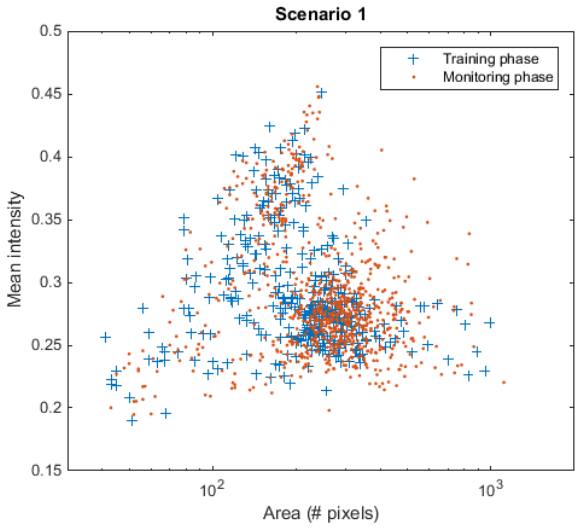

Fig. 8 – Scatterplot of the bivariate monitored descriptors in training phase and monitoring phase, Scenario 1.

A comparison between the data scatter in the training phase and the monitoring phase shows that the SLM process remained stable in Scenario 1 in terms of area and mean intensity of the ROI. This is coherent with the inspections and measurements performed on the produced

specimens. However, the non-normal distribution of the multivariate data implies the need to estimate the empirical distribution for control chart design as outlined in the next sub-section.

A bivariate control charting scheme can monitor the ROI stability over time and to automatically signal alarms in the presence of statistically significant departures from the training patterns. The proposed approach is based on the Hotelling's T^2 statistic [44], where the kernel density estimation (KDE) methodology [71] is used to cope with the non-normality of the monitored descriptors. The resulting control chart is also known as KDE-based T^2 chart [72]. The KDE allows one to express the control limit as the upper $100(1-\alpha)\%$ percentile of the fitted distribution of the T^2 statistic computed during the training phase where α is the Type I error. The Hotelling's T^2 statistic is defined as follows:

$$T_j^2 = \left(\boldsymbol{x}_j - \bar{\boldsymbol{x}}\right)^T \mathbf{S}^{-1}\left(\boldsymbol{x}_j - \bar{\boldsymbol{x}}\right), j = 1,2,\dots \quad (1)$$

where $\boldsymbol{x}_j = [A_j, \bar{I}_j]^T$ is the j-th bivariate vector of monitored descriptors, $\bar{\boldsymbol{x}}$ is the training sample mean vector, and $\mathbf{S}$ is the sample variance-covariance matrix of the training dataset $\mathbf{X} = [\boldsymbol{x}_1, \dots \boldsymbol{x}_j, \dots, \boldsymbol{x}_K]^T$. The matrix $\mathbf{S}$ is computed as follows: Let $\boldsymbol{v}_j = \boldsymbol{x}_{j+1} - \boldsymbol{x}_j, j = 1, \dots, K-1$, be the vector of successive differences, and let $\mathbf{V} = [\boldsymbol{v}_1, \dots \boldsymbol{v}_j, \dots, \boldsymbol{v}_{K-1}]$ be the matrix of successive difference vectors. The variance-covariance matrix estimator $\mathbf{S} = \frac{1}{2}[\mathbf{V}^T\mathbf{V}/(K-1)]$ is then used [73]. The KDE algorithm used here, a.k.a. unbiased cross-validation (UCV), is briefly reviewed in Appendix A.

Fig. 9 shows the resulting control chart for Scenario 1 where the training phase consists of four initial layers and the monitoring phase includes ten successive layers. The target Type I error was $\alpha = 0.01$. The control chart in Fig. 9 confirms the findings of inspections and measurements on the produced specimens, i.e., that the SLM in Scenario 1 was stable and representative of an in-control process.

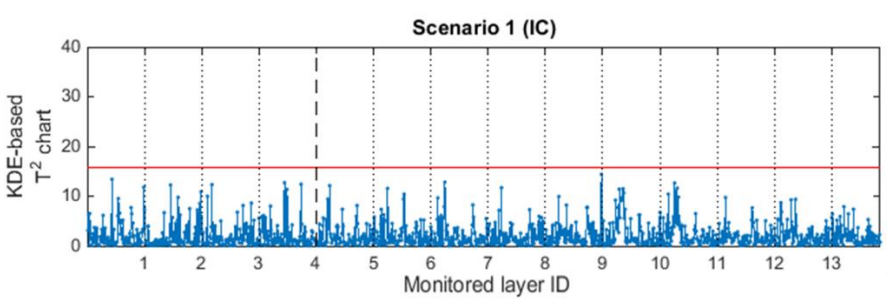

Fig. 9 – Proposed control charts in Scenario 1; the vertical dashed line separates the training phase from the monitoring phase; vertical dotted lines separate the monitored layers.

Although a plume-based monitoring approach has never been proposed in the SLM literature, two competitors were considered here as alternatives to our monitoring approach. The first simply consists of monitoring the mean pixel intensity of the original image without any segmentation operation (hereafter denoted as Competitor 1). This is representative of the simplest image-based monitoring approach for computationally efficient implementation in SLM applications. The descriptors refer to the entire video frame, and hence they are influenced not only by the presence of the plume, but also by the spatters and other hot spots that may originate during the process. Also, a KDE-based control limit estimation was adopted to monitor the statistical descriptor.

A second competitor is analogous to our proposed approach, but it skips the classification step to separate the ROI from the spatters; hence it applies the control charting scheme to all detected components in the IR images (Competitor 2). This is representative of a method that exploits the information coming from both the plume and the spatters without the need for any classification operation. The cumulative area of all the components in each frame and their mean intensity were used as statistical descriptors monitored via the KDE-based T^2 control chart.

Fig. 10 compares the control charts associated with the alternative methods in Scenario 1. Competitor 1 yields a false alarm rate larger than the target one, and the T^2 statistic also exhibits an autocorrelated and seasonal pattern that is caused by fluctuations of background intensities due to light reflections and spatters. The wild fluctuation of the spatter spread from one frame to another inflates the variability of the control statistic leading to a larger occurrence of false alarms under controlled conditions. In fact, the low sampling frequency ($f_s = 50\ Hz$) does not allow a proper characterization of the spatter kinematics, and this makes the presence of spatters a

nuisance factor rather than an additional information source. An analogous problem was observed in the case of Competitor 2 where the inclusion of the spatters into the monitored ROI generated a considerably skewed distribution of the T^2 statistic with a consequent increase of alarms under in-control conditions. The alarms signaled by the two competitors are false alarms because post-processing quality inspections on the specimens produced in Scenario 1 highlighted the absence of defects and process errors. This implies that the proposed approach should be preferred to the two considered competitors—it is more robust to nuisance factors and can properly capture the stability of the SLM process.

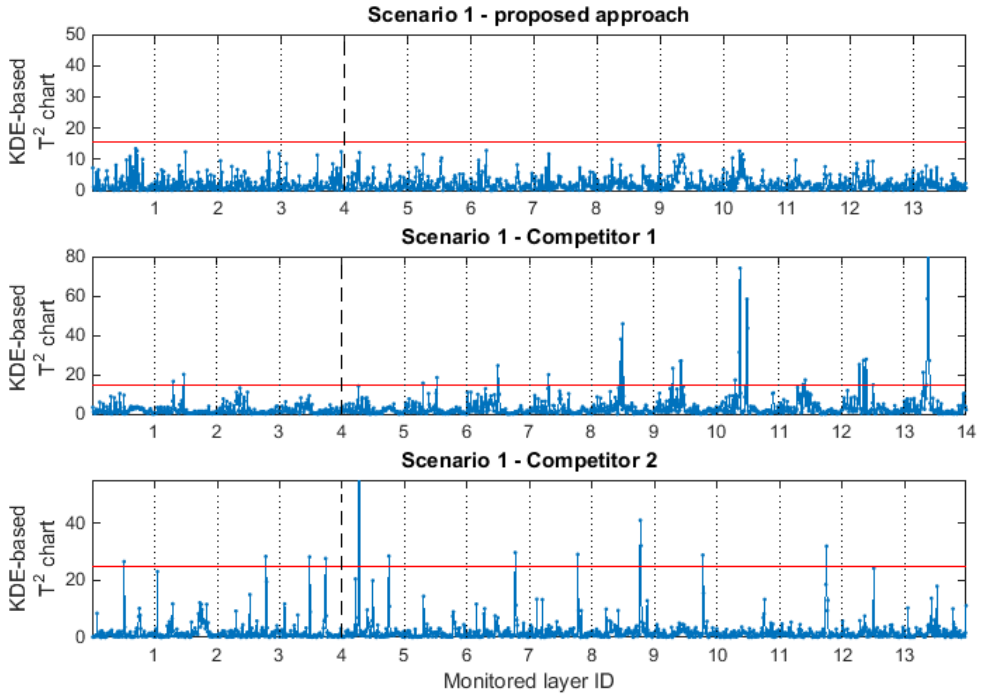

Fig. 10 – Top panel: proposed control chart in Scenario 1 (in-control); central and bottom panels: control charts corresponding to Competitor 1 and 2 in Scenario 1; vertical dashed lines separate the training phase from the monitoring phase; vertical dotted lines separate the monitored layers

4 Results and discussion

The results achieved by applying the proposed approach to Scenario 2 and 3 are discussed in sub-section 4.1 whereas sub-section 4.2 presents a sensitivity analysis of the control charts with respect to the choice of threshold S.

4.1 Process monitoring of Scenario 2 and 3

Fig. 11 shows a scatterplot of the bivariate data vectors $\boldsymbol{x}_j = [A_j, \overline{I}_j]^T$ belonging to the training set of Scenario 2 and 3 compared with the one in Scenario 1. The spread of the training data in Scenario 2 and 3 is considerably larger than in Scenario 1—especially regarding the area descriptor. This is related to the different energy densities associated with the choice of process parameters in those scenarios.

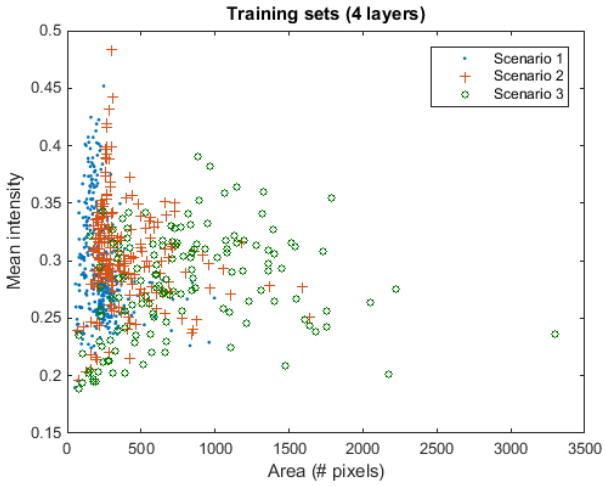

Fig. 11 – Scatterplot of the bivariate monitored descriptors acquired during the training phase in different scenarios.

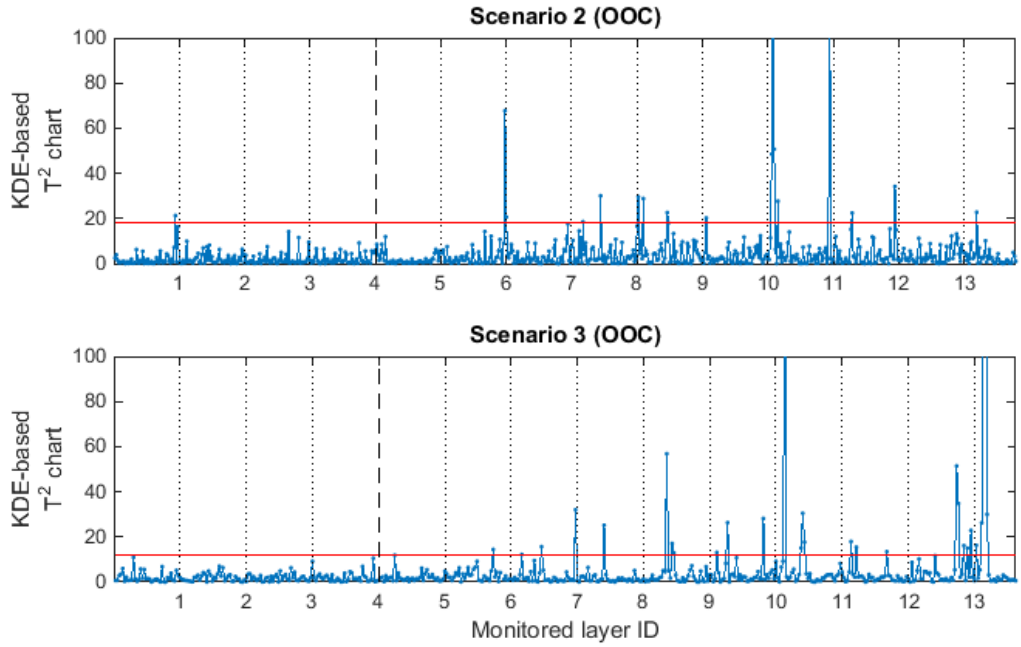

Fig. 12 – Top panel: Proposed control chart in Scenario 2 (out-of-control); Bottom panel: proposed control chart in Scenario 3 (out-of-control); vertical dashed lines separate the training phase from the monitoring phase; vertical dotted lines separate the monitored layers.

Fig. 12 shows the KDE-based T^2 control charts for Scenario 2 and 3. The target Type I error was $\alpha = 0.01$ in all scenarios. Fig. 12 shows that some instability originated during the process leading to an increasing occurrence of large T^2 peaks during the monitoring phase. This corresponds to anomalous values of the ROI descriptors. In particular, Scenario 2 has the largest peaks observed during the 11th monitored layer, but other control limit violations occurred starting from the 6th layer. In Scenario 3, a few out-of-control data points were signaled during the sixth and seventh monitored layer, but the frequency and severity of out-of-control signals grew over time. In this last scenario, the most severe peaks of the T^2 statistic correspond to the generation of large hot gas clouds in the 14th monitored layer similar to the ones produced by explosions. The most evident of these events are shown in Fig. 13—the ROI consists of a very large and hot region that moved towards the upper part of the IR image.

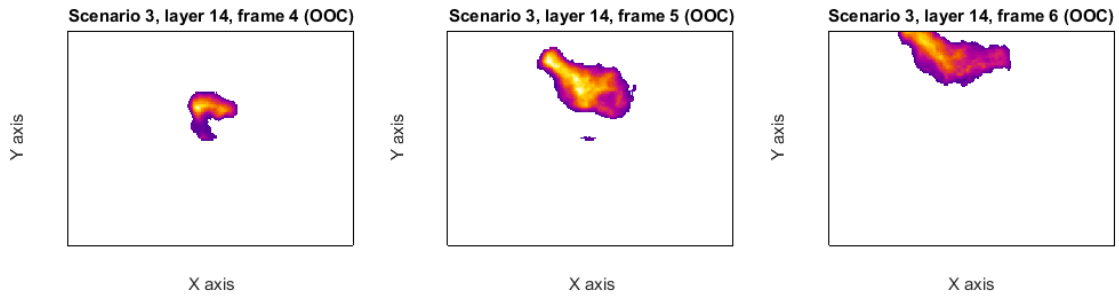

Fig. 13 – ROI extracted in three consecutive frames in Scenario 3 (14th monitored layer) signaled by the control chart as out-of-control.

The event depicted in Fig. 13 was the final result of an unstable melting condition that led to the disintegration of previously built layers. The onset of this instability was signaled by different layers in advance of the control chart. Considering that the monitored layers are spaced five layers apart, such an instable condition could be signaled at least 35 layers in advance with considerable material and time waste reduction if the process was stopped.

A further comparison between in-control and out-of-control scenarios is shown in Fig. 14. The sample mean and standard deviation of the T^2 statistic were computed in each layer, and the corresponding time-series plots are shown in Fig. 14. The first two moments of the T^2 distribution are stable over all the monitored layers in Scenario 1, which confirms the results discussed in the previous Section. In contrast, Scenario 2 and 3 show a trend of both the sample mean and sample standard deviation starting from the initial layers. This suggests that the Hotelling's T^2 statistic based on the descriptors of plume emissions is suitable to determine the stability of the SLM process and to anticipate the detection of out-of-control conditions. This is made possible by training the chart only on data acquired during the current process, i.e., the data acquired during a small number of initial layers even when the instability originates very early in the process.

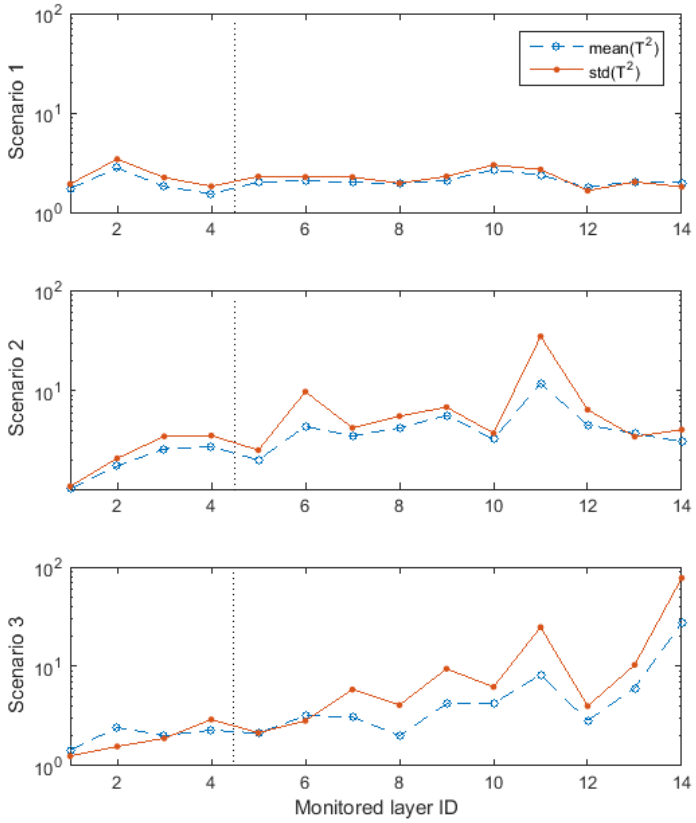

Fig. 14 – Top panel: Time-series of the sample mean and standard deviation of the T^2 statistic for all the monitored layers in Scenario 1. Central panel: Same time-series in Scenario 2. Bottom panel: Same time-series in Scenario 3; vertical dotted line separates training and monitoring phases.

Fig. 15 shows a scatterplot of the out-of-control observations signaled by the control charts in Scenario 2 (left panel) and Scenario 3 (right panel) superimposed on the training data. Fig. 15 shows the most important descriptor to detect the process instability is the plume area. Indeed, in both Scenario 2 and Scenario 3, the out-of-control states correspond to ROIs having a larger area than the one observed during the training phase. The contribution of the mean intensity descriptor, however, provides some additional information from a diagnostic viewpoint. The most severe out-of-control data in Scenario 2 corresponds to low intensity values. This is caused by an increase in the upper part of the plume where the intensity is lower than in the bottom part (the LHZ). On the contrary, Scenario 3 shows that the most severe out-of-control data corresponds to medium/high intensity values, which is caused by a different kind of event, i.e., the generation of large hot gas clouds as discussed above. Future studies may include additional statistical

descriptors of the selected ROI to get a deeper characterization of the plume emissions for diagnostic analysis.

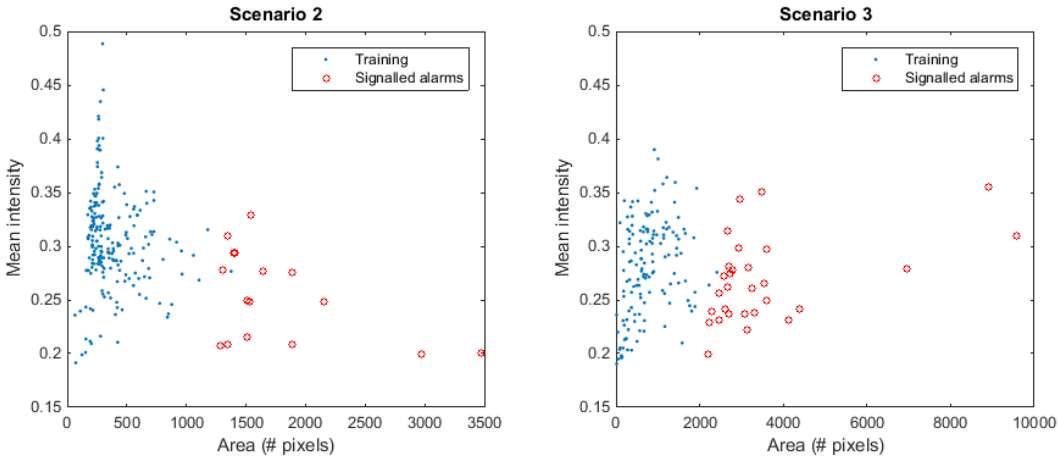

Fig. 15 – Scatterplot of training data and data signaled as out-of-control in Phase II, in Scenario 2 (left panel), and Scenario 3 (right panel).

4.2 Sensitivity analysis with respect to the threshold S

The threshold S determines which connected components are included into the ROI for process monitoring. An example of the sensitivity of the proposed control chart in Scenario 1 with respect to such a threshold is shown is Fig. 16 (the optimal choice based on the proposed technique was $S = 64$). Fig. 16 shows that the pattern of the monitored statistics is poorly affected by the choice of S in the range $45 \leq S \leq 85$, but for smaller values of S,the number and entities of data points above the control limit increases because of an increasing number of spatters included into the ROI. For $S = 0$, the control chart coincides with the one called "Competitor 2", i.e., the competitor that includes all foreground connected components into the ROI. Indeed, no classification is applied when $S = 0$.

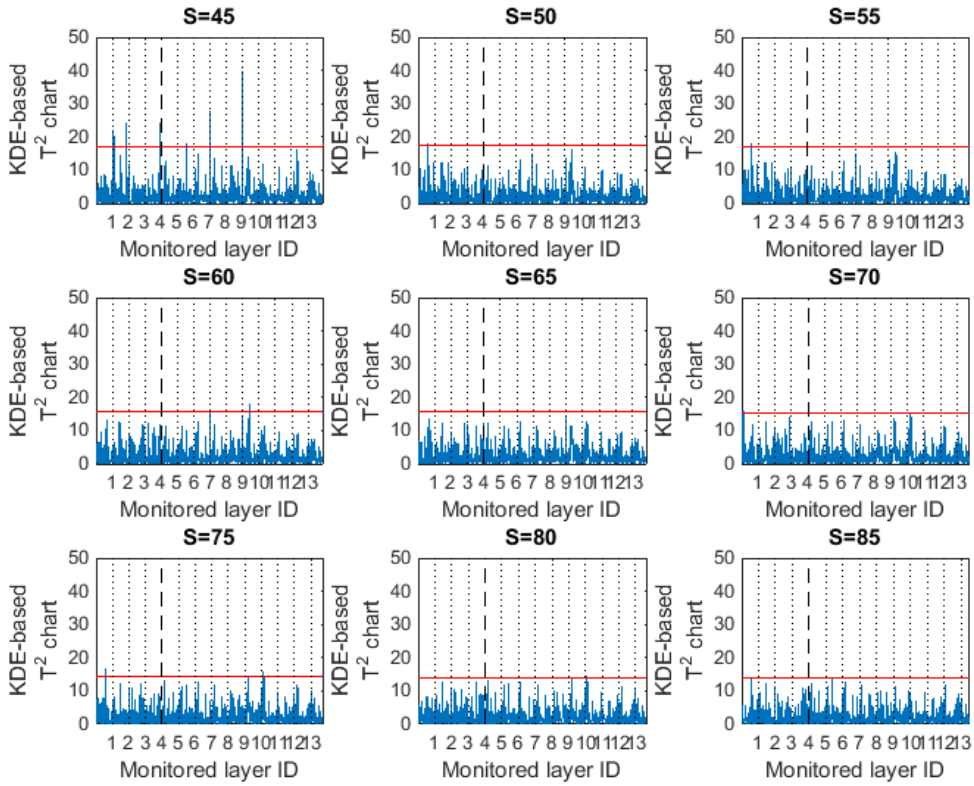

Fig. 16 – Proposed control charts in Scenario 1 corresponding to different choices of the threshold *S*.

5 Conclusion

The improvement of the process capability and stability in SLM still deserves research efforts to meet challenging industrial requirements. Different kinds of defects may originate during the layer-wise production of the part with a detrimental impact on its geometrical or mechanical/physical properties. Higher complexity values of produced shapes and structures result in worse inspectability of the defects. This pushes the need for in-process monitoring solutions. This study determined the suitability of the plume properties as signatures of the SLM process stability. A case study of SLM on zinc powder was presented, which involves both stable and unstable melting conditions. A particular defect type was found in the processing of zinc and was related to partial disintegration due to excessive heat accumulation. The proposed approach exploits IR images acquired with an off-axial IR camera to detect possible deviations from a stable behavior since their early stage. The underlying idea is that the statistical descriptors of the plume should be stable over time under in-control conditions. Thus, a small number of initial layers can

be used to characterize the dynamic behavior of the process in terms of measurable signatures and to design a control chart (training phase) that will be applied to any successive layer of the same process.

We proposed an automated rule to extract the region of interest from each monitored image such that only the relevant portion of the video frame may be used for monitoring purposes. The area and mean intensity of the same region can then be monitored via a T^2 control chart. A comparison analysis showed that the proposed approach is more effective than monitoring the original IR frames without any segmentation and/or ROI identification. The study also showed that the proposed method is robust to the choice of the threshold adopted to separate the ROI from other foreground features, i.e., the spatters.

Future developments will verify the suitability and the performances of the proposed approach for image streams acquired with a different frame rate or with a different experimental setup. Generally speaking, ex-ante or external information about the laser trajectory can be integrated into the monitoring scheme to enhance the process behavior characterization and to link the estimated signatures to known process dynamics. Future research efforts will be aimed at facing these issues.

Acknowledgments

This work was supported by Regione Lombardia under the call “Creatività: Eventi e Luoghi per L’innovazione nella Moda e nel Design, Linea 2: Infrastrutturazione Fisica e Digitale”.

Nomenclature

α	Type I error
A_j	Area of the ROI in the j-th video frame
f_s	Sampling frequency
$f(x)$	Probability density function
h	Kernel bandwidth
IC	In-control
I	Pixel intensity

$\overline{I_J}$	Average intensity of the ROI in the j-th video frame
IR	Infrared
J	Total number of acquired images
K	Number of frames included into the training phase
KDE	Kernel density estimation
$Ker\{x\}$	Kernel function
$M \times N$	Size of IR images
n_j	Number of pixels of the ROI in the j-th video frame
OOC	Out-of-control
$P_1(S)$	% of frames with more than one connected component classified as ROI
$P_2(S)$	% of frames with more no connected component was classified as ROI
RGB	Red green blue
ROI	Region of interest
S	Area threshold
$\mathbf{S}$	Sample variance-covariance matrix
SLM	Selective laser melting
LHZ	Laser heated zone
T	Binarization threshold
T^2	Hotelling's statistic
$\boldsymbol{\mathcal{U}}$	3-dimensional array representing the IR image stream
$\boldsymbol{U}_j$	j-th IR video frame
UCV	Unbiased cross-validation
$\mathbf{V}$	Matrix of successive difference vectors
$\boldsymbol{x}_j$	Bi-variate monitored variable
$\mathbf{X}$	Training dataset (monitored descriptors)

References

[1] Gibson, I., Rosen, D. W., Stucker, B. 2010. "Additive manufacturing technologies". New York: Springer.

[2] Horn, T. J., Harrysson, O. L. 2012. "Overview of current additive manufacturing technologies and selected applications". Science progress, 95(3), pp. 255-282.

[3] Mellor, S., Hao, L., Zhang, D. 2014. "Additive manufacturing: A framework for implementation". International Journal of Production Economics, 149, pp. 194-201.

[4] Olakanmi, E. O., Cochrane, R. F., Dalgarno, K. W. 2015. "A review on selective laser sintering/melting (SLS/SLM) of aluminium alloy powders: Processing, microstructure, and properties". Progress in Materials Science, 74, pp. 401-477

[5] Zhang, B., & Coddet, C. 2016. "Selective laser melting of iron powder: observation of melting mechanism and densification behavior via point-track-surface-part research". Journal of Manufacturing Science and Engineering,138(5), pp. 051001 – 05001-9.

[6] Frazier, W. E. 2014. "Metal additive manufacturing: A review". Journal of Materials Engineering and Performance, 23(6), pp. 1917-1928.

[7] Zhang, L. C., Attar, H. 2015. "Selective Laser Melting of Titanium Alloys and Titanium Matrix Composites for Biomedical Applications: A Review". Advanced Engineering Materials, DOI: 10.1002/adem.201500419

[8] Chua, C. K., Leong, K. F., Liu, Z. H. 2015. "Rapid Tooling in Manufacturing". In Handbook of Manufacturing Engineering and Technology (pp. 2525-2549). Springer London.

[9] Habib, M.A., Khoda, B., 2017, Attribute driven process architecture for additive manufacturing, Robotics and Computer-Integrated Manufacturing, 44, 253-265

[10] Tapia, G., Elwany, A. 2014. "A Review on Process Monitoring and Control in Metal-Based Additive Manufacturing". Journal of Manufacturing Science and Engineering, 136(6), pp. 060801.

[11] Mani, M., Lane, B., Donmez, A., Feng, S., Moylan, S., & Fesperman, R. 2015. "Measurement Science Needs for Real-time Control of Additive Manufacturing Powder Bed Fusion Processes", NISTIR 8036, http://dx.doi.org/10.6028/NIST.IR.8036

[12] Grasso, M., Colosimo, B.M., 2017. Process Defects and In-situ Monitoring Methods in Metal Powder Bed Fusion: a Review, Measurement Science and Technology, https://doi.org/10.1088/1361-6501/aa5c4f

[13] Everton, S. K., Hirsch, M., Stravroulakis, P., Leach, R. K., & Clare, A. T. (2016). Review of in-situ process monitoring and in-situ metrology for metal additive manufacturing. Materials & Design, 95, 431-445.

[14] Sames, W. J., List, F. A., Pannala, S., Dehoff, R. R., & Babu, S. S. (2016). The metallurgy and processing science of metal additive manufacturing. International Materials Reviews, 1-46.

[15] Spears, T. G., & Gold, S. A. (2016). In-process sensing in selective laser melting (SLM) additive manufacturing. Integrating Materials and Manufacturing Innovation, 5(1), 1.

[16] Clijsters, S., Craeghs, T., Buls, S., Kempen, K., & Kruth, J. P. (2014). In situ quality control of the selective laser melting process using a high-speed, real-time melt pool monitoring system. The International Journal of Advanced Manufacturing Technology, 75(5-8), 1089-1101.

[17] Craeghs, T., Bechmann, F., Berumen, S., & Kruth, J. P. (2010). Feedback control of Layerwise Laser Melting using optical sensors. Physics Procedia, 5, 505-514.

[18] Craeghs, T., Clijsters, S., Kruth, J. P., Bechmann, F., & Ebert, M. C. (2012). Detection of process failures in layerwise laser melting with optical process monitoring. Physics Procedia, 39, 753-759.

[19] Craeghs, T., Clijsters, S., Yasa, E., Bechmann, F., Berumen, S., & Kruth, J. P. (2011). Determination of geometrical factors in Layerwise Laser Melting using optical process monitoring. Optics and Lasers in Engineering, 49(12), 1440-1446.

[20] Berumen, S., Bechmann, F., Lindner, S., Kruth, J. P., & Craeghs, T. (2010). Quality control of laser-and powder bed-based Additive Manufacturing (AM) technologies. Physics procedia, 5, 617-622.

[21] Kruth, J. P., Mercelis, P., Van Vaerenbergh, J., & Craeghs, T. (2007). Feedback control of selective laser melting. In Proceedings of the 3rd international conference on advanced research in virtual and rapid prototyping (pp. 521-527).

[22] Van Gestel, C. (2015). Study of physical phenomena of selective laser melting towards increased productivity. PhD Dissertation, Ecole Polytechnique Federale De Lausanne

[23] Lott, P., Schleifenbaum, H., Meiners, W., Wissenbach, K., Hinke, C., & Bültmann, J. (2011). Design of an optical system for the in situ process monitoring of selective laser melting (SLM). Physics Procedia, 12, 683-690.

[24] Chivel, Y. (2013). Optical in-process temperature monitoring of selective laser melting. Physics Procedia, 41, 904-910.

[25] Doubenskaia, M., Pavlov, M., Grigoriev, S., Tikhonova, E., & Smurov, I. (2012). Comprehensive optical monitoring of selective laser melting. Journal of Laser Micro Nanoengineering, 7(3), 236-243.

[26] Pavlov, M., Doubenskaia, M., & Smurov, I. (2010). Pyrometric analysis of thermal processes in SLM technology. Physics Procedia, 5, 523-531.

[27] Thombansen, U., Gatej, A., & Pereira, M. (2015). Process observation in fiber laser–based selective laser melting. Optical Engineering, 54(1), 011008-011008.

[28] Yadroitsev, I., Krakhmalev, P., & Yadroitsava, I. (2014). Selective laser melting of Ti6Al4V alloy for biomedical applications: Temperature monitoring and microstructural evolution. Journal of Alloys and Compounds, 583, 404-409.

[29] Kanko, J. A., Sibley, A. P., & Fraser, J. M. (2016). In situ morphology-based defect detection of selective laser melting through inline coherent imaging. Journal of Materials Processing Technology, 231, 488-500.

[30] Grasso, M., Laguzza, V., Semeraro, Q., & Colosimo, B. M. (2016). In-process Monitoring of Selective Laser Melting: Spatial Detection of Defects via Image Data Analysis. Journal of Manufacturing Science and Engineering, 139(5), 051001-1 – 051001-16.

[31] Krauss, H., Eschey, C., & Zaeh, M. (2012). Thermography for monitoring the selective laser melting process. In Proceedings of the Solid Freeform Fabrication Symposium.

[32] Krauss, H., Zeugner, T., & Zaeh, M. F. (2014). Layerwise monitoring of the selective laser melting process by thermography. Physics Procedia, 56, 64-71.

[33] Lane, B., Moylan, S., Whitenton, E. P., & Ma, L. (2015). Thermographic Measurements of the Commercial Laser Powder Bed Fusion Process at NIST. In Proc. Solid Free. Fabr. Symp (Vol. 575).

[34] Bayle, F., & Doubenskaia, M. (2008). Selective laser melting process monitoring with high speed infra-red camera and pyrometer. In Fundamentals of Laser Assisted Micro-and Nanotechnologies (pp. 698505-698505). International Society for Optics and Photonics.

[35] Schilp, J., Seidel, C., Krauss, H., & Weirather, J. (2014). Investigations on temperature fields during laser beam melting by means of process monitoring and multiscale process modelling. Advances in Mechanical Engineering, 6, 217584.

[36] Neef, A., Seyda, V., Herzog, D., Emmelmann, C., Schönleber, M., & Kogel-Hollacher, M. (2014). Low coherence interferometry in selective laser melting. Physics Procedia, 56, 82-89.

[37] Foster, B. K., Reutzel, E. W., Nassar, A. R., Hall, B. T., Brown, S. W., & Dickman, C. J. (2015) Optical, layerwise monitoring of powder bed fusion. In Solid Free. Fabr. Symp. Proc, 295-307.

[38] Zur Jacobsmühlen, J., Kleszczynski, S., Schneider, D., & Witt, G. (2013). High resolution imaging for inspection of laser beam melting systems. In 2013 IEEE International Instrumentation and Measurement Technology Conference (I2MTC) (pp. 707-712). IEEE.

[39] Kleszczynski, S., zur Jacobsmühlen, J., Sehrt, J. T., & Witt, G. (2012). Error detection in laser beam melting systems by high resolution imaging. In Proceedings of the Solid Freeform Fabrication Symposium.

[40] Zhang, B., Ziegert, J., Farahi, F., & Davies, A. (2016). In situ surface topography of laser powder bed fusion using fringe projection. Additive Manufacturing, 12, 100-107.

[41] Mireles, J., Ridwan, S., Morton, P. A., Hinojos, A., & Wicker, R. B. (2015). Analysis and correction of defects within parts fabricated using powder bed fusion technology. Surface Topography: Metrology and Properties, 3(3), 034002.

[42] Wegner, A., & Witt, G. (2011). Process monitoring in laser sintering using thermal imaging. In SFF Symposium, Austin, Texas, USA (pp. 8-10).

[43] Islam, M., Purtonen, T., Piili, H., Salminen, A., & Nyrhilä, O. (2013). Temperature profile and imaging analysis of laser additive manufacturing of stainless steel. Physics Procedia, 41, 835-842.

[44] Montgomery, D. C. 2009. Statistical quality control (Vol. 7). New York: Wiley.

[45] P. K. Bowen, J. Drelich, J. Goldman, 2013, Zinc exhibits ideal physiological corrosion behavior for bioabsorbable stents. Adv. Mater., 25(18), 2577-2582

[46] King, W.E., Barth, H.D., Castillo, V.M., Gallegos, G.F., Gibbs, J.W., Hahn, D.E., Kamath, C., Rubenchik, A.M., 2014. Observation of keyhole-mode laser melting in laser powder-bed fusion additive manufacturing. J. Mater. Process. Technol., vol. 214, no. 12, pp. 2915–2925, 2014.

[47] Chun-Ming Wang, Xuan-Xuan Meng, Wei Huang, Xi-Yuan Hu, Ai-Qin Duan, 2011 , Role of side assisting gas on plasma and energy transmission during CO2 laser welding , Journal of Materials Processing Technology, 211, 668–674

[48] Montani M, Demir AG, Mostaed E, 2016. Processability of pure Zn and pure Fe by SLM for biodegradable metallic implant manufacturing, Rapid Prototyping Journal, Accepted article, 10.1108/RPJ-08-2015-0100

[49] Gao, X. D., Wen, Q., Katayama, S. 2013. Analysis of high-power disk laser welding stability based on classification of plume and spatter characteristics, Transactions of Nonferrous Metals Society of China, 23(12), 3748-3757

[50] Wen, Q., Gao, X. D. 2012. Classification of Plume Image and Analysis of Welding Stability during High Power Disc Laser Welding, Applied Mechanics and Materials, 201-202, 1139-1142

[51] Zhang, J., Chen, G. Y., Zhou, Y., Li, S. C., Deng, H. 2013. Observation of spatter formation mechanisms in high-power fiber laser welding of thick plate, Applied Surface Science, 280, 868-875

[52] Colombo, D., Colosimo, B. M., & Previtali, B., 2013, Comparison of methods for data analysis in the remote monitoring of remote laser welding. Optics and Lasers in Engineering, 51(1), 34-46.

[53] Nassar, A.R., Spurgeon, T.J. and Reutzel, E.W. 2014. Sensing defects during directed-energy additive manufacturing of metal parts using optical emissions spectroscopy, Solid Freeform Fabrication Symposium Proceedings, University of Texas, Austin, TX.

[54] Mumtaz, K., Hopkinson, N. 2010. Selective laser melting of thin wall parts using pulse shaping, Journal of Materials Processing Technology, 210(2), 279-287

[55] Y. F. Zheng, X. N. Gu, and F. Witte, 2014, Biodegradable metals, Mater. Sci. Eng. R Reports, 77, 1–34

[56] Demir, A. G., Monguzzi, L., & Previtali, B. (2017). Selective laser melting of pure Zn with high density for biodegradable implant manufacturing. Additive Manufacturing, 15, 20-28.

[57] Repossini, G., Laguzza, V., Grasso, M., & Colosimo, B. M. (2017). On the use of spatter signature for in-situ Monitoring of Laser Power Bed Fusion. Additive Manufacturing, 16, 35-48, https://doi.org/10.1016/j.addma.2017.05.004

[58] Sezgin, M., Sankur, B 2004, Survey over image thresholding techniques and quantitative performance evaluation. Journal of Electronic imaging, 13(1), 146-168.

[59] Chaki, N., Hossain Shaikh, S., Saeed, K. 2014, Exploring Image Binarization Techniques, Vol. 560 of the series Studies in Computational Intelligence, 5-15

[60] Cheng, H. D., Jiang, X. H., Sun, Y., Wang, J. 2001. Color image segmentation: advances and prospects. Pattern recognition, 34(12), 2259-2281.

[61] Ridler, T.W. Calvard, S. 1978, Picture thresholding using an iterative selection method, IEEE Transactions on Systems, Man and Cybernetics 8: 630-632

[62] Otsu, N., 1979, A Threshold Selection Method from Gray-Level Histograms, IEEE Transactions on Systems, Man, and Cybernetics, 9(1), 62-66

[63] Li, C.H. Tam, P.K.S. 1998, An Iterative Algorithm for Minimum Cross Entropy Thresholding, Pattern Recognition Letters 18(8): 771-776

[64] Huang, L.-K. Wang, M.-J. J. 1995, Image thresholding by minimizing the measure of fuzziness, Pattern Recognition 28(1): 41-51

[65] Hastie, T., Tibshirani, R., Friedman, J. 2009. The elements of statistical learning, 2(1). Springer, New York

[66] Liu, D., Yu, J. 2009, Otsu method and K-means. In HIS'09 Ninth International Conference on Hybrid Intelligent Systems, August 2009, 1, 344-349

[67] Fabbro, R., Coste, F., Goebels, D., Kielwasser, M., 2006. Study of CW Nd-YAG laser welding of Zn-coated steel sheets. J. Phys. D. Appl. Phys. 39,.401–409.

[68] Kaplan, A. F. H., Mizutani, M., Katayama, S., Matsunawa, A., 2002. Unbounded keyhole collapse and bubble formation during pulsed laser interaction with liquid zinc. J. Phys. D. Appl. Phys. 35. 1218–1228

[69] Wang, C. M., Meng, X. X., Huang, W., Hu, X. Y., & Duan, A. Q. (2011). Role of side assisting gas on plasma and energy transmission during CO 2 laser welding. Journal of Materials Processing Technology, 211(4), 668-674.

[70] Colombo, P., Demir, A. G., Norgia, M., & Previtali, B. (2017). Self-mixing interferometry as a diagnostics tool for plasma characteristics in laser microdrilling. Optics and Lasers in Engineering, 92, 17-28.

[71] Bowman, A. W., Azzalini A. 1997. Applied Smoothing Techniques for Data Analysis, Oxford University Press, New York

[72] Chou, Y-M., Mason, R.L., Young J.C. 2001. The Control Chart for Individual Observations from A Multivariate Non-normal Distribution. Communications in Statistics, Simulation and Computation, 30(8–9), 1937–1949

[73] Williams, J. D., Woodall, W. H., Birch, J. B., and Sullivan, J. H. 2006. On the Distribution of Hotelling's T2 Statistic based on the Successive Differences Covariance Matrix Estimator, Journal of Quality Technology, 38, 217-229

[74] Hardle, W., Marron, J. S., Wand, M. P., 1990, Bandwidth choice for density derivatives, Journal of the Royal Statistical Society. Series B (Methodological), pp. 223-232.

Appendix A – The Unbiased Cross-Validation procedure

KDE algorithms share the same underlying idea, i.e., fitting the density function $f(x)$ of a random variable x at a point x_i using the neighbouring observations such that the influence of x_i on the estimate at any x vanishes asymptotically. The kernel estimator of the probability density function $f(x)$ is given by [74]:

$$\hat{f}(x) = K^{-1}\sum_{j=1}^{K} h^{-1}Ker\{(x - T_j^2)/h\} \tag{A1}$$

Two relevant issues consist of the choice of the kernel function, $Ker\{x\}$, and the selection of an optimal kernel bandwidth, h. The most common choice for the kernel function consists of the Gaussian radial basis function, RBF, whereas the choice of the bandwidth is more critical. The essential idea of UCV is to use the bandwidth, $\hat{h}$, which minimizes the function:

$$UCV(\hat{h}) = \int \hat{f}_{\hat{h}}(x)^2 dx - \frac{2}{K}\sum\nolimits_j \hat{f}_{\hat{h},j}(T_j^2) \tag{A2}$$

Here, $\hat{f}_{\hat{h}}$ denotes the kernel estimator based on the choice $\hat{h}$, and $\hat{f}_{\hat{h},j}$ denotes the leave-one-out kernel estimator defined as follows:

$$\hat{f}_{\hat{h},j}(x) = (K-1)^{-1} \sum_{\substack{u=1 \\ u \neq j}}^{K} h^{-1} Ker\{(x - T_u^2) / \hat{h}\} \quad \text{(A3)}$$

Thus, the optimal choice $\hat{h}$ is defined by:

$$\hat{h} = arg \min_{h>0} UCV(h) \quad \text{(A4)}$$